ACS NANO

www.acsnano.org

ARTICLE

Dimension Engineering of Boron Nitride Nanostructures through Catalytic Flash Joule Heating

Jinhang Chen,[#] Yi Cheng,[*,#] Phelecia Scotland, Jaeho Shin, Lorenzo Castelli, John Tianci Li, Weiyin Chen, Kevin M. Wyss, Qiming Liu, Obinna E. Onah, Geoff Wehmeyer, Yufeng Zhao,[*] and James M. Tour[*]

Cite This: https://doi.org/10.1021/acsnano.5c03593 **Read Online**

ACCESS | Metrics & More | Article Recommendations | Supporting Information

ABSTRACT: **Boron nitride (BN) is well-known for its excellent thermal conductivity, high chemical stability, and low dielectric constant, making it widely used as a lubricant, thermal management material, and electrical insulator. For different applications, the nanostructure of BN plays a prominent role. In particular, boron nitride nanotubes (BNNTs) are preferred for enhancing the properties in specific directions. Traditional BNNT synthetic methods often require valuable precursors and catalysts and prolonged reaction time for structure engineering, limiting their practical applications. Here, we present a dimension engineering strategy to controllably synthesize one-dimensional BNNTs and two-dimensional nanosheets (BNNSs) by flash Joule heating (FJH) within 1 min. The scalable production of ~5 g is achieved per batch. During BN synthesis, sulfur is identified as a crucial additive that accelerates precursor dehydration and facilitates nanotube formation. When applied as additives in composites, BNNTs exhibit enhanced mechanical strength and thermal conductivity compared to BNNSs, highlighting the necessity of BN dimension engineering for diverse applications. This work offers a feasible strategy for tailoring BN nanostructures and optimizing their properties, with potential applicability in the synthesis of other nanomaterials beyond BN.**

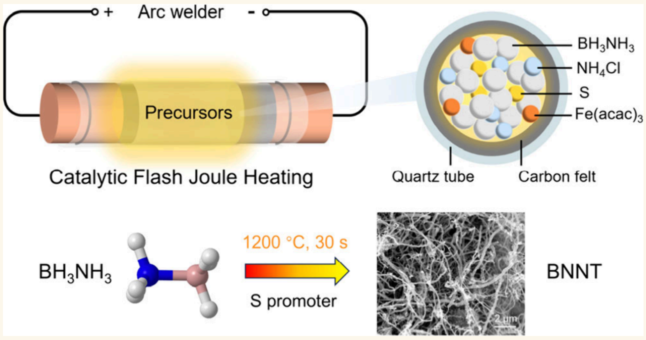

KEYWORDS: *boron nitride nanotube, boron nitride nanosheet, dimension engineering, flash Joule heating, catalytic growth*

Boron nitride (BN), with its high thermal conductivity,[1] chemical inertness,[2] excellent mechanical strength,[3] and electrical insulation,[4] has been widely recognized as a promising material for reinforcement,[5] lubrication,[6] thermal management,[7,8] neutron shielding,[9] and optoelectronic[10] applications. Composed of sp^2-hybridized B and N atoms as fundamental building blocks, hexagonal BN (h-BN) can be assembled into different dimensional forms, including one-dimensional (1D) boron nitride nanotubes (BNNTs) and two-dimensional (2D) boron nitride nanosheets (BNNSs). The variation in dimensionality introduces distinct interfacial interactions and functional properties, making them suitable for different applications. For example, the planar symmetry of BNNSs enables uniform in-plane properties, making them ideal for dielectric layers and 2D devices.[11] In contrast, BNNTs, with their distinct strength, flexibility, and through-plane load transfer, are commonly employed as reinforcements in composite materials.[12] Therefore, dimension engineering is a crucial prerequisite for tailoring BN materials to meet specific application requirements.

A variety of synthesis methods have been explored to fabricate BN nanostructures with a controlled dimensionality. Mechanical exfoliation is a feasible approach for high-quality, ultrathin BNNSs, though only in limited quantities.[13] For scalable production, liquid-phase exfoliation is commonly employed, but it offers limited control over BNNS thickness and morphology.[14] Chemical vapor deposition (CVD) is the most widely adopted technique for the BN synthesis. Without specific control, 2D BN films are commonly grown on Cu or

Received: February 27, 2025
Revised: June 16, 2025
Accepted: June 17, 2025

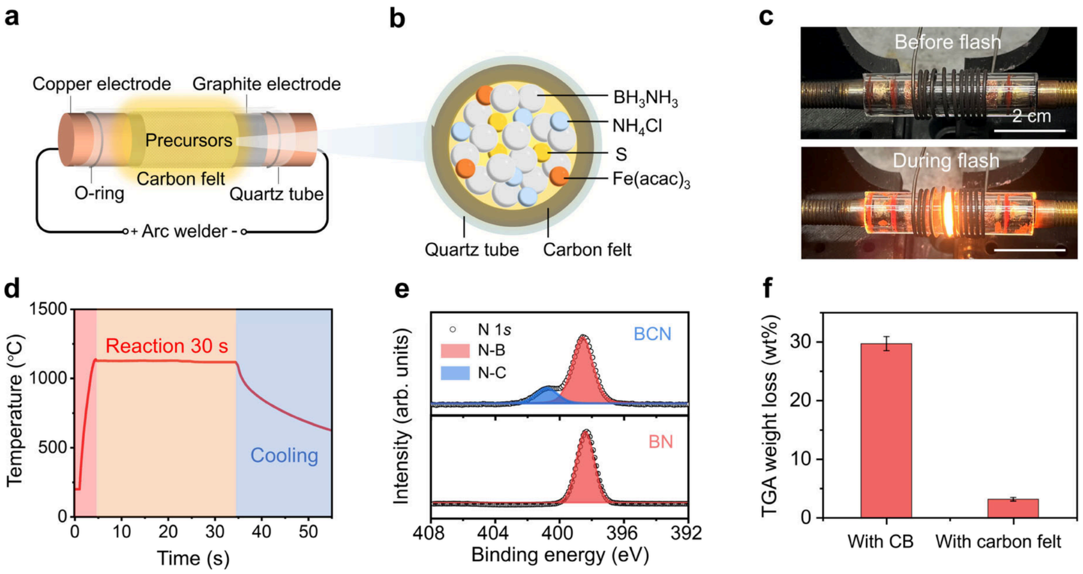

Figure 1. FJH setup for BN synthesis using carbon felt as the heating element. (a) Schematic diagram of the FJH setup. (b) Cross-sectional schematic illustrating the use of carbon felt in FJH. (c) Pictures of reactors (i) before and (ii) during the FJH process. A spring coiled around the tube surface enhances the mechanical integrity of the tube reactor. (d) Real-time temperature profile with an input current of 30 A during FJH. (e) N 1s XPS spectra of flash-synthesized BN with carbon black as the conducting additive (termed BCN) and with carbon felt as the heating element (termed as BN). (f) Weight loss of the flashed BCN and BN tested by TGA. TGA tests were conducted in a 100 mL min^{-1} air flow with a heating rate of 10 °C min^{-1}. Error bars represent standard deviations from three parallel tests.

Ni substrates using borazine or ammonia boron.[15] For 1D BNNTs synthesis, expensive B/N sources and catalysts, precise control of gas flow and temperature, and extended reaction durations are often required. Despite these efforts, precursor conversion efficiency and overall production scalability remain limited, hindering the practical deployment of BNNTs.[16,17] Therefore, developing accessible synthesis methods that combine cost-effectiveness, scalability, and precise dimensional control is essential for advancing BN nanostructure applications.

Flash Joule heating (FJH) induces localized heating and rapidly reaches high temperatures within seconds, making it a promising technique for nanomaterial synthesis with low energy consumption and good controllability.[18−23] Here, we developed a sulfur-promoted strategy for the selective synthesis of BNNTs and BNNSs using FJH. During the FJH process, ammonia borane (AB) and iron(III) acetylacetonate ($Fe(acac)_3$) served as the precursor and catalyst, respectively, while ammonium chloride was employed to mitigate nitrogen loss. Sulfur was introduced as a selectivity promoter, facilitating AB dehydration and nanotube formation. Using carbon felt as the heating element, BNNT and BNNS were selectively synthesized using a commercial arc welder within 1 min with low carbon impurities. The selectivity for each BN nanostructure reached >60%. When used as composite additives, BNNTs demonstrated enhanced thermal conductivity, modulus, and hardness, compared with BNNSs, highlighting the advantages of dimension engineering in improving composite performance. This study presents an energy-efficient strategy for BN nanostructure synthesis, enabling precise dimensional control for targeted applications. The insights gained into the catalytic growth process during rapid electrical heating provide a valuable foundation for advancing nanomaterial synthesis techniques.

RESULTS AND DISCUSSION

In a typical FJH process, a mixture of AB, $Fe(acac)_3$, NH_4Cl, and S is embedded in a curved carbon felt and then compressed inside a quartz tube between two graphite rods (Figure 1a). The carbon felt served as the heating element, while a commercial arc welder provided a continuous power supply. During FJH, the carbon felt was rapidly heated and transferred heat to the precursors, initiating BN growth as the current passed through (Figure 1b). Benefiting from a stable current input, the reaction temperature was maintained at ∼1200 °C for 30 s, with a low variation of <3% (Figure 1d). By adjustment of the input current from 10 to 70 A, the reaction temperature was precisely controlled between 750 and 2100 °C (Figure S1).

For the flash of nonconductive precursors, carbon additives, such as carbon black powder, are often required to ensure the sample conductivity.[24−26] However, during BN synthesis, carbon reacts with the precursors, leading to undesirable carbon doping in the flashed product (termed flash BCN) and influencing its purity. Distinct C−N (∼286.0 eV) and N−C (∼400.7 eV) peaks were observed in the C 1s and N 1s X-ray photoelectron spectra (XPS), respectively (Figure 1e and Figures S2 and S3). Due to the formation of C−N bonds, excess boron interacts with residual oxygen, as evidenced by the B−O peak at ∼193.1 eV (Figure S2). A weight loss of 29.7 wt % was observed in BCN samples by thermogravimetric analysis (TGA, Figure 1f and Figure S4), mainly attributed to carbon removal. To address the issue, we applied a high-temperature-stable carbon felt as the heating element to minimize the carbon contact with the precursor, thereby reducing carbon impurities in flash-synthesized BN. As a result, the C−N, N−C, and B−O peaks in flashed BN samples disappeared, and the weight loss decreased to 3.1 wt % (Figure 1e,f and Figures S2−S4).

During BN synthesis, when AB was directly used as the precursor, the B/N mole ratio in the flashed BN was often >1,

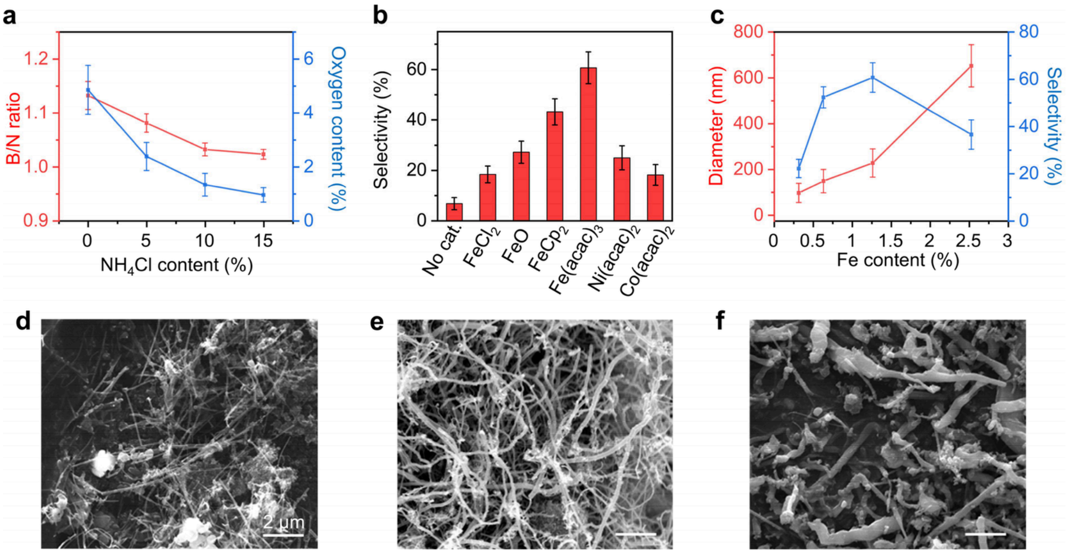

Figure 2. Parameter modulation for dimension engineering during BN synthesis. (a) B/N mole ratios and oxygen contents in BN products with the increase of NH_4Cl contents in the precursors. (b) Nanotube selectivity using different catalysts. The catalyst metal content is kept at 1.3 wt %. (c) Diameter and selectivity of flash-synthesized BNNT with different Fe catalyst content. Error bars in (a) represent standard deviations from three parallel XPS tests. Error bars of the selectivity in (b) and (c) represent standard deviations from three samples under the same reaction conditions. Error bars of tube diameter in (c) represent standard deviations from 50 nanotubes from 10 SEM images. (d–f) SEM images of BNNT synthesized with Fe catalyst content of (d) 0.3 wt %, (e) 1.3 wt %, (f) 2.5 wt %.

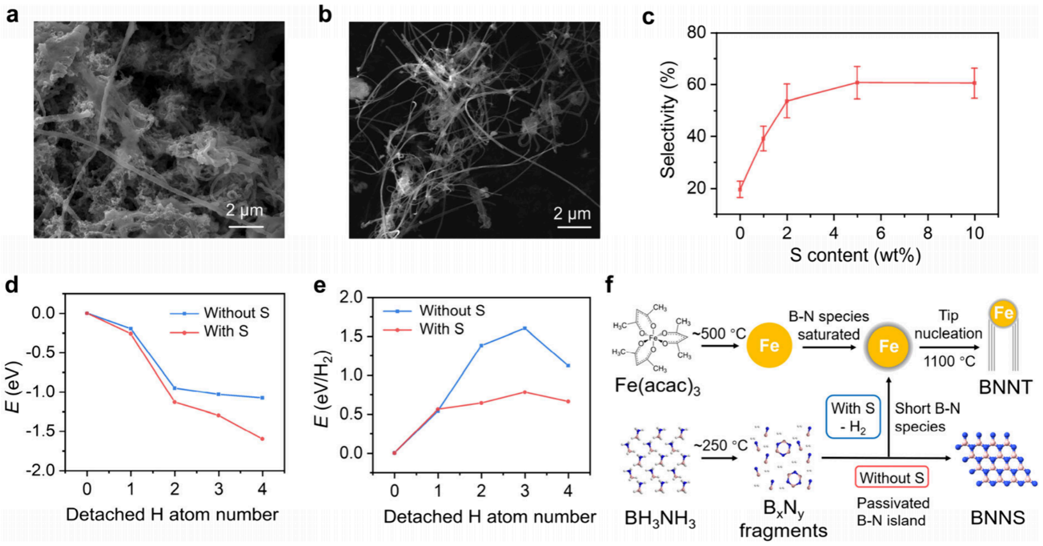

Figure 3. Influence of sulfur on BNNT synthesis. (a, b) SEM images of BNNT (a) without sulfur and (b) with 5 wt % sulfur. (c) Nanotube selectivity with the increase of sulfur content. Error bars of the selectivity represent standard deviations from three samples under the same reaction conditions. (d) Total energy change in the sequence of H atoms being detached from the AB molecules and transferred to the Fe surface. (e) Desorption energy of hydrogen from the Fe (100) surface after each H atom is detached from the AB molecule. (f) Reaction mechanism of sulfur-promoted BNNT growth.

which can be ascribed to the higher vapor pressure of N compared to B (Figure S5). Excessive B tended to bond with oxygen, leading to oxygen impurities (Figure S6). To mitigate nitrogen loss, NH_4Cl was introduced into the precursor, generating NH_3 to react with boron compounds during the reaction. As the NH_4Cl content increased from 0 to 15 wt %, the B/N mole ratio gradually decreased from 1.13 to 1.02, while the oxygen content was reduced from 4.9 to 1.0 at% (Figure 2a and Figure S7), indicating improved purity of the flashed BN products.

In order to achieve dimension engineering of the flashed products, especially to increase the BNNT selectivity while maintaining a high yield, we first optimized the reaction temperature and duration. Yield was defined as the mass of flash-synthesized BN products divided by theoretical yield based on the AB amount, while selectivity was determined by calculating the proportion of BNNT-dominant images among 50 scanning electron microscopy (SEM) images. Generally, higher reaction temperatures and longer reaction durations improved BNNT selectivity but reduced the overall yield (Figure S8). The optimized conditions were set to 1200 °C for 30 s, achieving ~60.7% nanotube selectivity with a high yield of ~67.2% (Figure S9). During the synthesis process, the catalyst is another prominent factor influencing BN structures.

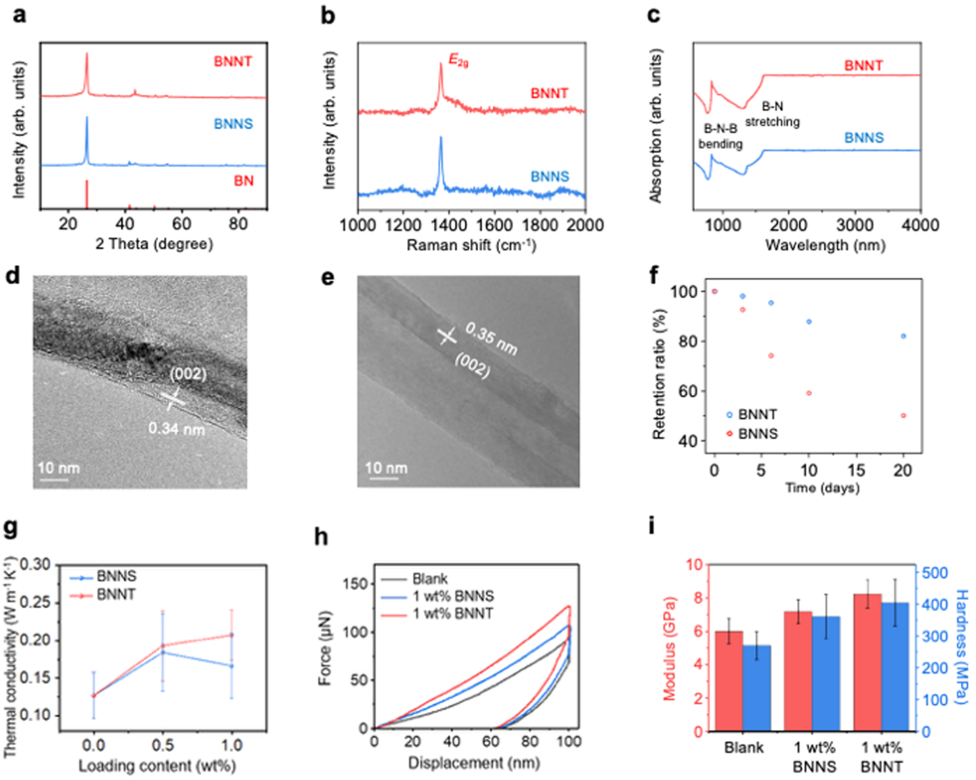

Figure 4. Comparisons between BNNS and BNNT. (a) XRD patterns of BNNS (blue line) and BNNT (red line). The PDF card for h-BN is 00-015-0500. (b) Raman spectra of BNNS (blue line) and BNNT (red line). (c) Infrared spectra of BNNS (blue line) and BNNT (red line). (d, e) TEM images of (d) BNNS and (e) BNNT. (f) Retention percentage of commercial BNNS (blue) and BNNT (red) after different sedimentation times. (g) Thermal conductivities of VER composites with different contents of BNNT (red line) and BNNS (blue line) additives. (h) Force−displacement curves of VER composites obtained from nanoindentation tests under different loads. (i) Modulus and hardness of blank VER, and VER with 1 wt % BNNS, and 1 wt % BNNT. Error bars in (g) represent standard deviations from three parallel tests. Error bars in (i) represent standard deviations from 10 parallel tests.

Without any catalyst, BNNS tended to be formed with high uniformity (Figure S10), while introducing catalysts would lead to nanotube structure formation. Among various Fe compounds, Fe(acac)$_3$ was identified as the best catalyst, achieving a selectivity of 60.7%, followed by ferrocene (denoted as FeCp$_2$, ∼43.2%). In comparison, FeO and FeCl$_2$ showed much lower selectivity (<30%, Figure 2b). This can be attributed to the low decomposition temperature of Fe(acac)$_3$ (∼190−275 °C, Table S1), which enables the rapid formation of a high concentration of catalytic metal nanoparticles. We then compared the catalytic performance of different transition metal acetylacetonates, where Fe(acac)$_3$ demonstrated higher selectivity than its Ni and Co counterparts. When further modulating the Fe catalyst content, BNNT selectivity increased but decreased with excessive catalyst amounts. The optimal catalyst concentration was 1.3 wt % (Figure 2c). The increase in the catalyst content also led to a larger BNNT diameter, likely due to the aggregation of catalytic metal cores (Figure 2d−f).

Moreover, in our experiment, we found that sulfur is a crucial additive for nanotube formation. With 5 wt % sulfur, BNNT selectivity increased from 19.5% to 60.7% (Figure 3a,b). However, further increasing the sulfur content to 10 wt % does not lead to an obvious change in selectivity (Figure 3c). To better understand the role of sulfur in catalytic growth, we conducted theoretical simulations to reveal the dehydrogenation process of the AB precursor on the Fe (100) surface (see details in Note S1 and Figures S11 and S12). The energy continuously decreased at each dehydration step, indicating that the stepwise detachment of H atoms from AB on the Fe (100) surface was energetically favorable. The sulfur atoms on the Fe surface destabilized Fe−H binding, lowering the dehydrogenation energy of AB to form BN. Then, we calculated the desorption energy of the H atoms from the Fe surface sequentially after their detachment from the AB molecule. Except for the first H atom, the desorption energy of the remaining three decreased by 50% in the presence of sulfur (Figure 3e and Table S2), indicating that sulfur substantially accelerates hydrogen desorption. Slow hydrogen desorption leads to rapid saturation and passivation of edge atoms, limiting the supply of B−N species and favoring BNNS growth via surface-mediated deposition. In contrast, fast hydrogen desorption promotes further dehydration and rapid release of HB-NH building units, facilitating catalyst-mediated nucleation and BNNT growth.[27] The increased availability of B−N species due to H_2 removal aligns with Le Chatelier's principle, based on the equation of $BH_3NH_3(g) \rightarrow BN(s) + 3H_2(g)$.[28]

The reaction mechanism of sulfur-promoted BNNT growth is summarized in Figure 3f. Catalytic BNNT growth in FJH follows a tip-growth model via the vapor−liquid−solid (VLS) mechanism, as evidenced by the TEM images (Figure S13). This behavior is consistent with observations from the boron oxide CVD (BOCVD) method.[14,29] At the reaction temperature, Fe nanoparticles react with B or B−N species and partially melt at the surface, forming an amorphous transition layer. The rapidly released B−N species then diffuse into the condensed Fe catalyst, leading to saturation and subsequent BNNT precipitation.[13] In this process, sulfur accelerates H_2 dissociation on the Fe surface and facilitates the direct fusion of adjacent BN ring networks on the catalyst surface.[28,30]

For practical applications of flash-synthesized BN materials, we demonstrated the scalability of the FJH methods using a 16 mm quartz tube (Figure S14a,b). During FJH, the temperature showed negligible variations (<5%) along the tube axis (Figure S14c,d), confirming temperature stability for uniform sample heating. ∼5 g of BNNT was successfully synthesized with high selectivity (Figure S14e). To withstand a higher pressure during the reaction, especially in scale-up processes, thick-walled polyether ether ketone (PEEK) tubing can be used (Figure S15). Benefiting from our experiences in scaling up the FJH process, kilogram-scale graphene production has already been achieved in a laboratory reaction system,[31] and tonne/day industrially,[32] which is ready to be applied for BN synthesis. In addition to its scalability, the FJH method offers higher selectivity and yield, lower energy consumption, and significantly shorter reaction times compared to those of other BNNT synthesis methods (Table S3). While CVD is commonly used for gram-scale BNNT production and operates at reaction temperatures comparable to those of a similar gas-phase growth mechanism, FJH achieves substantially shorter reaction durations and higher yields (Table S4), making it a promising alternative for efficient and scalable BNNT synthesis.

Meanwhile, considering the presence of NH_4Cl, S, and $Fe(acac)_3$ in the precursor mixture, potential impurities from Cl, S, and Fe could affect the performance of the flashed products. Due to the low decomposition temperature of NH_4Cl, Cl content in the flashed products was negligible (<0.1 at%) in the flashed products (Figure S16). However, a distinct sulfur content of ∼3.1 atom % was observed (Figure S17). TGA results showed that the sulfur oxidation occurred within the 200−350 °C (Figure S18). Since carbon oxidation occurs at 600 °C (Figure S4), we calcined the flashed BN samples at 600 °C for 30 min in the air. Negligible sulfur or carbon signals were detected after calcination (Figures S19 and S20), while BN remained unchanged (Figures S21 and S22), confirming the effective removal of both carbon and sulfur impurities through this process. Note that a portion of the trace C (∼1 atom %) in the calcined products may result from the adsorption of hydrocarbons from the laboratory air. In contrast, flashed BCN samples exhibited inferior thermal stability and were oxidized to B_2O_3 in air, due to the loss of carbon sites during calcination (Figures S21 and S22). For the Fe residues, initial Fe contents in the precursors were measured to be ∼1.3 wt % by inductively coupled plasma mass spectroscopy (ICP-MS). After the flash, the residue Fe content decreased to ∼0.7 wt %. After leaching with 1 M HCl, a substantial amount of Fe residue (∼850 ppm) remained in the flashed samples. However, after the calcination steps for sulfur removal, followed by the same acid-leaching process, the Fe residue content further decreased to ∼100 ppm, making it suitable for further applications (Figure S23).

After sample purification, we conducted characterizations to compare the morphologies and properties of the BNNT and BNNS. X-ray diffraction (XRD) analysis revealed the characteristic (002) diffraction peak of h-BN in both BNNT and BNNS samples (Figure 4a).[32] Notably, BNNTs exhibited a lower (002) peak position (∼25.6°) compared to BNNSs (∼26.2°) in the high-resolution scans (Figure S24), and both were lower than that of bulk h-BN (∼26.6°), indicating an expanded interlayer spacing.[33,34] In the Raman spectra (Figure 4b), the E_{2g} peaks of both BNNT and BNNS appeared at ∼1366 cm^{-1} with a narrow distribution (Figure S25), consistent with bulk h-BN (1365−1366 cm^{-1}).[34,35] The domain size of tens of nanometers is confirmed by the broadening of XRD and Raman peaks (see details in Note S2), attributed to the ultrafast reaction kinetics of the FJH process.[24] The Fourier transform infrared (FTIR) spectrum further confirmed BN structures, showing a B−N stretching peak at 1320 cm^{-1} and a B−N−B bending peak at 765 cm^{-1} for both BNNT and BNNS (Figure 4c).[35] The broadened FTIR signals are attributed to nanoscale crystalline domains and weakened vibrational coupling compared to bulk h-BN.[36]

High-resolution transmission electron microscopy (HRTEM) confirmed the high crystallinity of BNNS, with a lattice spacing of ∼0.34 nm corresponding to the (002) facet of BN (Figure 4d).[37] BNNT exhibited a hollow tubular structure, and its lattice spacing of ∼0.35 nm was slightly larger than that of BNNS (Figure 4e).[38] Both values are consistent with the estimates based on the (002) XRD peak position (Note S2) and are higher than the lattice spacing of 0.33 nm for bulk h-BN, indicating a weakened interlayer interaction. High-angle annular dark-field scanning transmission electron microscopy (HAADF-STEM) and energy-dispersive X-ray spectroscopy (EDS) verified the uniform distribution of B and N elements, showing well-overlapped elemental mapping in both BNNS and BNNT (Figure S26). Atomic force microscopy (AFM) further confirmed the tubular and sheet-like morphologies of BNNT and BNNS, respectively (Figure S27). The measured thickness of BNNSs (∼35 nm) is consistent with the distribution of 38.4 ± 4.7 nm derived from the SEM results (Figure S10).

In addition, BNNT exhibited a higher surface area (∼150 m^2 g^{-1}) than BNNS (∼89 m^2 g^{-1}), attributed to its smaller size and high aspect ratio (Figure S28), which contributed to its lower thermal stability in air (Figure S29). When dispersed in a 1 wt % Pluronic F-127 aqueous solution, both BNNT and BNNS demonstrated good dispersion (Figure S30), ascribed to the expanded interlayer spacing and weaker interactions. Notably, BNNT showed a much better dispersion retention of ∼83% than BNNS (∼50%) after 20 days (Figure 4f).

Benefiting from their high aspect ratios and excellent dispersion stability, BNNTs were used as additives for vinyl ester resin (VER) composites. As the BNNT content increased from 0 to 1 wt %, the thermal conductivity of VER increased from 0.13 to 0.21 W m^{-1} K^{-1}. In contrast, when BNNS was used as the additive, the thermal conductivity of VER initially increased but then decreased with a loading content of 1 wt %, likely due to BNNS agglomeration (Figure 4g). We further evaluated the mechanical properties of VER composites by using nanoindentation. With 1 wt % BNNT loading, VER composites exhibited an average modulus of 8.2 GPa and an average hardness of 404.7 MPa, demonstrating notable improvement compared to VER composites with 1 wt % BNNS (modulus, 7.2 GPa; hardness, 361.6 MPa, Figure 4h,i). In addition, the flash-synthesized BNNTs exhibit improved thermal and mechanical property enhancements when incorporated into composites, outperforming other BN-based additives reported in the literature (Tables S5 and S6). These findings underscore their exceptional reinforcing efficiency and

https://doi.org/10.1021/acsnano.5c03593

strong potential as high-performance nanofillers for advanced composite applications.

CONCLUSION

This work presents a sulfur-promoted strategy for engineering the dimensionality of BN via catalytic FJH. The introduction of sulfur facilitates precursor dehydrogenation and hydrogen desorption on the catalyst surface, enabling precise control over BNNT formation with high selectivity (>60%) and yield (>60%) while achieving a record-high production rate exceeding 1 g/min. When incorporated into polymer composites, the synthesized BNNTs provided distinct enhancements in both thermal and mechanical properties compared to BNNSs, underscoring the importance of dimensionality control in nanostructures for targeted applications. This efficient and scalable synthesis strategy holds great promise as a versatile platform for tailoring nanomaterial structure and expanding their application potential.

EXPERIMENTAL METHODS

Materials. Quartz tubing (8 mm inner diameter) was used for the reaction with a batch size of 500 mg. Ammonia borane (97%), NH_4Cl (99.5%), sulfur (99.98% trace metals basis), Fe(III) acetylacetonate (99%), Ni(II) acetylacetonate (95%), Co(II) acetylacetonate (97%), $FeCl_2 \cdot 4H_2O$ (98%), and FeO (10 mesh, 99.6% trace metals basis) were purchased from Millipore-Sigma. Pluronic acid F-127 was obtained from BASF.

Flash Joule Heating Process. Carbon felt (3.1 mm thickness, Fuel Cell Store) was used for the heater and cut with an areal size of 2 cm × 2.5 cm. AB (stored in an Ar-filled glovebox, $O_2 < 0.5$ ppm, $H_2O < 0.5$ ppm), NH_4Cl, $Fe(acac)_3$, and sulfur are mixed and subsequently embedded within the carbon felt. The optimal mass ratio among AB, NH_4Cl, $Fe(acac)_3$, and sulfur is 72:15:8:5. The precursor-loaded carbon felt was placed inside an 8 mm diameter quartz tube, covering the tube inner surface. Graphite rods served as electrodes at both ends of the tube with copper wool positioned between the graphite rods and the flash electrodes to enhance electrical contact. The sample resistance was modulated to ~0.5 Ω. The tube was then positioned on a custom-built reaction jig, sealed with two O-rings on each side, and connected to an external arc welder system. During the flash process, a steady current passed through the carbon felt, heating the embedded precursors. The heating temperature was regulated by controlling the input current, and the heating duration was manually controlled by switching the beaker of the power supply. The flash temperature was recorded by an infrared (IR) thermometer (Micro-Epsilon) in the detecting range of 200−1500 °C with a detection interval of 1 ms. After flashing, the samples rapidly cooled to room temperature.

Dispersion Test. BNNS and BNNT (2−10 mg mL^{-1}) were dispersed into an aqueous solution of Pluronic F-127 (1 wt % in deionized water), respectively, and subjected to sonication (DUC-1002-00, CREWORKS) for 30 min. The supernatant was then analyzed via UV−vis spectroscopy based on the Lambert−Beer law. To determine the BN concentration, the dispersions were diluted 100 fold, and the absorbance was measured at 300 nm. An extinction coefficient of $\alpha_{300} = 3177$ L g^{-1} m^{-1} was applied for concentration.[39]

Composite Preparations. For vinyl ester resin (VER) preparation, 5 g of vinyl ester (VE, Fiberglass Supply Depot) was placed in a 20 mL scintillation vial, followed by the gradual addition of BN at varying loadings from 0.5 to 1 wt %. The mixture was stirred at room temperature using a magnetic stir bar at 300 rpm for 30 min and then subjected to ultrasonication (DUC-1002-00, CREWORKS) for another 30 min. Subsequently, shear mixing was performed using a homogenizer (Cole-Parmer Tissue Tearor 986370-07, 120 VAC, 1.2 A) at 10000 rpm for 3 min. Methyl ethyl ketone peroxide (MEKP, Fiberglass Supply Depot) was then added as a hardener at 3 wt % and mixed via shear mixing at 9000 rpm for 1 min, followed by mechanical stirring at 300 rpm for 5 min. The composite was left to cure overnight in a scintillation vial before being removed for thermal conductivity testing.

Thermal Conductivity Test. During the thermal conductivity measurements, the temperature gradient along the *Z*-axis was recorded by using four thermocouples positioned on each side of the composite sample. The temperature data were linearly fitted to minimize the squared error, enabling the determination of the heat flow. The uncertainties in both the heat flow and temperature differentials across the sample were obtained through this fitting process. The cross-sectional area of the sample was calculated from its volume-to-thickness ratio.

Nanoindentation Test. Nanoindentation was performed by using displacement-controlled nanoindentation (Hysitron TI 980 Triboindenter), where the indentation depth was maintained at 100 nm for 10 s before initiating the unloading phase. This hold period minimizes dynamic effects and ensures the load stability. By allowing stress redistribution, the hold period ensures that the material fully responds to the indentation, which is crucial for soft materials, thin films, and porous structures where initial loading effects can skew results. After the hold period, the indenter was smoothly retracted to evaluate the material's elastic recovery and accurately determine mechanical properties, including hardness and reduced elastic modulus, which were calculated as the average of 10 collected data points. The elastic modulus and hardness were determined using the Oliver−Pharr method, based on eqs 1−3.[40]

$$E_r = \frac{\sqrt{\pi}}{2}\frac{S}{\sqrt{A_P}} \tag{1}$$

$$\frac{1}{E_r} = \frac{1 - \nu^2}{E} + \frac{1 - \nu_i^2}{E_i} \tag{2}$$

$$H = \frac{P}{A_P} \tag{3}$$

where E_r is the reduced elastic modulus; S is the stiffness derived from the initial part of the unloading curve; A_P is the projected contact area; E and ν are the elastic modulus and Poisson's ratio of the sample, respectively; E_i and ν_i are the elastic modulus and Poisson's ratio of the indenter, respectively; H is the hardness; and P is the applied load.

Characterization. XRD was performed using a Rigaku SmartLab system with filtered Cu Kα radiation (λ = 1.5406 Å). FT-IR spectra were obtained with a Thermo Scientific Nicolet 6700 attenuated total reflectance FTIR (ATR-FTIR) spectrometer (Waltham, MA, USA). XPS was conducted using a PHI Quantera XPS system under a pressure of 5×10^{-9} Torr. Survey spectra were collected with a step size of 0.5 eV and a pass energy of 140 eV, while elemental spectra were acquired with a step size of 0.1 eV and a pass energy of 26 eV. A Shirley-type background was subtracted as the baseline, and peak fitting was performed by using a Lorentzian−Gaussian mixed function. All XPS spectra were calibrated using the C 1*s* peak at 284.8 eV as a reference. SEM imaging and elemental analysis via EDS were performed on an FEI Quanta 400 ESEM FEG system at an accelerating voltage of 10 kV and a working distance of 10 mm. TGA was carried out using the Mettler Toledo TGA/DSC 3+ system at a heating rate of 10 °C·min^{-1} under an air or N_2 flow of 100 mL·min^{-1}. HRTEM images were acquired on a JEOL 2100 field emission gun transmission electron microscope operated at 200 kV. HAADF-STEM imaging and EDS mapping were performed using an FEI Titan Themis3 system equipped with image and probe aberration corrections and an electron monochromator operating at 80 kV. The AFM test was conducted in noncontact mode using a Park NX20 system (Park Systems Corp., South Korea). A PPP-NCHR cantilever was employed with a spring constant (k) of 42 N m^{-1} and a resonance frequency (f) of 330 kHz. Before imaging, BNNT samples were sonicated in isopropanol for 30 min (DUC-1002-00 CREWORKS), and then cast onto a SiO_2 (300 nm)/Si substrate, while BNNS samples were prepared using mechanical exfoliation onto a SiO_2 (300 nm)/Si substrate. UV−vis spectroscopy was conducted by using a

Shimadzu UV-3600 Plus spectrophotometer. Brunauer−Emmett−Teller (BET) measurements were conducted at 77 K using a Quantachrome Autosorb-iQ3-MP/Kr BET analyzer with nitrogen as the adsorption/desorption gas. To determine the iron impurity content, 30 mg of the sample was digested in a mixture of HNO_3 (67−70 wt %, TraceMetal grade, Fisher Chemical) and HCl (37 wt %, 99.99% trace-metal basis, MilliporeSigma) at a 1:3 volume ratio. The digestion process was carried out in a PerkinElmer MPS320 microwave digestion system for 1 h. After digestion, the solution was filtered through a 0.22 μm polyether sulfone membrane and subsequently diluted with 2 wt % HNO_3 to align with the calibration curve range (1−100 ppb). Iron quantification was performed using a PerkinElmer Nexion 300 ICP-MS.

ASSOCIATED CONTENT

Supporting Information

The Supporting Information is available free of charge at https://pubs.acs.org/doi/10.1021/acsnano.5c03593.

> DFT computational details; interlayer spacing and crystallite size analysis; detailed characterizations of flash-synthesized BNNTs and BNNSs, including XPS, TGA, ICP-MS, SEM, TEM, other spectra and images; and tables for methods and material performance comparison (PDF)

AUTHOR INFORMATION

Corresponding Authors

Yi Cheng − *Department of Chemistry, Rice University, Houston, Texas 77005, United States;* orcid.org/0000-0002-5865-0685; Email: yi.cheng@rice.edu

Yufeng Zhao − *Department of Materials Science and NanoEngineering, Rice University, Houston, Texas 77005, United States; Corban University, Salem, Oregon 97317, United States;* Email: YZhao@rice.edu

James M. Tour − *Department of Chemistry, Department of Materials Science and NanoEngineering, Applied Physics Program and Smalley-Curl Institute, and NanoCarbon Center and the Rice Advanced Materials Institute, Rice University, Houston, Texas 77005, United States;* orcid.org/0000-0002-8479-9328; Email: tour@rice.edu

Authors

Jinhang Chen − *Department of Chemistry, Rice University, Houston, Texas 77005, United States*

Phelecia Scotland − *Department of Chemistry and Department of Materials Science and NanoEngineering, Rice University, Houston, Texas 77005, United States*

Jaeho Shin − *Department of Chemistry, Rice University, Houston, Texas 77005, United States*

Lorenzo Castelli − *Department of Mechanical Engineering, Rice University, Houston, Texas 77005, United States*

John Tianci Li − *Department of Chemistry, Rice University, Houston, Texas 77005, United States;* orcid.org/0000-0002-7218-8298

Weiyin Chen − *Department of Chemistry, Rice University, Houston, Texas 77005, United States;* orcid.org/0000-0002-6427-4129

Kevin M. Wyss − *Department of Chemistry, Rice University, Houston, Texas 77005, United States*

Qiming Liu − *Department of Chemistry, Rice University, Houston, Texas 77005, United States;* orcid.org/0000-0001-5839-5453

Obinna E. Onah − *Department of Chemistry and Department of Mechanical Engineering, Rice University, Houston, Texas 77005, United States;* orcid.org/0000-0001-8985-582X

Geoff Wehmeyer − *Department of Mechanical Engineering, Rice University, Houston, Texas 77005, United States;* orcid.org/0000-0002-6764-7744

Complete contact information is available at: https://pubs.acs.org/10.1021/acsnano.5c03593

Author Contributions

[#]J.C. and Y.C. contributed equally to this work.

Notes

The authors declare the following competing financial interest(s): Rice University owns intellectual property on the flash Joule heating strategy. J.M.T. is a shareholder in a company that licensed the intellectual property from Rice University. J.M.T. is not an officer, director, or employee of the company. All conflicts of interest are managed through regular disclosure to and compliance with the Rice University Office of Sponsored Programs and Research Compliance.

ACKNOWLEDGMENTS

The funding for the research is provided by the Air Force Office of Scientific Research (Grant FA9550-22-1-0526, J.M.T.), the U.S. Army Corps of Engineers ERDC (Grant W912HZ-21-2-0050, J.M.T.), and Rice Academy Fellowship (Y.C.). The authors acknowledge the use of the Electron Microscopy Center (EMC) at Rice University. The characterization equipment used in this project is from the Shared Equipment Authority (SEA) at Rice University. The authors thank Dr. Bo Chen of Rice University for the helpful discussion of the XPS results.

REFERENCES

(1) Cai, Q.; Scullion, D.; Gan, W.; Falin, A.; Zhang, S.; Watanabe, K.; Taniguchi, T.; Chen, Y.; Santos, E. J. G.; Li, L. H. High Thermal Conductivity of High-Quality Monolayer Boron Nitride and Its Thermal Expansion. *Sci. Adv.* **2019**, *5*, No. eaav0129.

(2) Zhou, Z.; Zhang, K.; Xiao, G.; Wang, Y.; He, Q.; Wang, N.; Wu, L.; Yao, Y. Surface Growth of Boron Nitride Nanotubes through Boron Source Design. *Adv. Funct. Mater.* **2023**, *33*, 2304450.

(3) Falin, A.; Cai, Q.; Santos, E. J. G.; Scullion, D.; Qian, D.; Zhang, R.; Yang, Z.; Huang, S.; Watanabe, K.; Taniguchi, T.; Barnett, M. R.; Chen, Y.; Ruoff, R. S.; Li, L. H. Mechanical Properties of Atomically Thin Boron Nitride and the Role of Interlayer Interactions. *Nat. Commun.* **2017**, *8*, 15815.

(4) Maruyama, S.; Arnold, M. S.; Krupke, R.; Peng, L.-M. Physics and Applications of Nanotubes. *J. Appl. Phys.* **2022**, *131*, No. 080401.

(5) Zhi, C.; Bando, Y.; Tang, C.; Kuwahara, H.; Golberg, D. Large-Scale Fabrication of Boron Nitride Nanosheets and Their Utilization in Polymeric Composites with Improved Thermal and Mechanical Properties. *Adv. Mater.* **2009**, *21*, 2889−2893.

(6) Wu, H.; Yin, S.; Du, Y.; Wang, L.; Yang, Y.; Wang, H. Alkyl-Functionalized Boron Nitride Nanosheets as Lubricant Additives. *ACS Appl. Nano Mater.* **2020**, *3*, 9108−9116.

(7) Hu, J.; Huang, Y.; Yao, Y.; Pan, G.; Sun, J.; Zeng, X.; Sun, R.; Xu, J.-B.; Song, B.; Wong, C.-P. Polymer Composite with Improved Thermal Conductivity by Constructing a Hierarchically Ordered Three-Dimensional Interconnected Network of BN. *ACS Appl. Mater. Interfaces* **2017**, *9*, 13544−13553.

(8) Liu, Y.; Zhao, N.; Xu, J. Mechanically Strong and Flame-Retardant PBO/BN/MXene Nanocomposite Paper with Low Thermal Expansion Coefficient, for Efficient EMI Shielding and Heat Dissipation. *Adv. Fiber Mater.* **2023**, *5*, 1657−1670.

(9) Ryu, K.-H.; Kang, M.; Kim, J.; You, N.-H.; Jang, S. G.; Jeong, K.-U.; Ahn, S.; Kim, D.-Y. Spacesuit Textiles from Extreme Fabric Materials: Aromatic Amide Polymer and Boron Nitride Nanotube Composite Fiber for Neutron Shielding and Thermal Management. *Adv. Fiber Mater.* **2024**, *6*, 1509−1520.

(10) Ma, C.; Ma, C.; Liu, C.; Guo, Q.; Huang, C.; Yao, G.; Li, M.; Qi, J.; Qin, B.; Sui, X.; Li, J.; Wu, M.; Gao, P.; Wang, W.; Bai, X.; Sun, Z.; Wang, E.; Hong, H.; Liu, K. Strong Chiroptical Nonlinearity in Coherently Stacked Boron Nitride Nanotubes. *Nat. Nanotechnol.* **2024**, *19*, 1299−1305.

(11) Orikasa, K.; Benedetti, L.; Chu, S.-H.; Dolmetsch, T.; Jimenez, A.; John, D.; Smith, T.; Thomas, T.; Boesl, B.; Park, C.; Agarwal, A. The Shape Effect: Influence of 1D and 2D Boron Nitride Nanostructures on the Radiation Shielding, Thermal, and Damping Properties of High-Temperature Epoxy Composites. *Compos. Sci. Technol.* **2025**, *261*, 110995.

(12) Wadhwa, G. K.; Late, D. J.; Charhate, S.; Sankhyan, S. B. 1D and 2D Boron Nitride Nano Structures: A Critical Analysis for Emerging Applications in the Field of Nanocomposites. *ACS Omega* **2024**, *9*, 26737−26761.

(13) Pacilé, D.; Meyer, J. C.; Girit, Ç. Ö.; Zettl, A. The Two-Dimensional Phase of Boron Nitride: Few-Atomic-Layer Sheets and Suspended Membranes. *Appl. Phys. Lett.* **2008**, *92*, 133107.

(14) Bari, R.; Parviz, D.; Khabaz, F.; Klaassen, C. D.; Metzler, S. D.; Hansen, M. J.; Khare, R.; Green, M. J. Liquid Phase Exfoliation and Crumpling of Inorganic Nanosheets. *Phys. Chem. Chem. Phys.* **2015**, *17*, 9383−9393.

(15) Yuan, Y.; Weber, J.; Li, J.; Tian, B.; Ma, Y.; Zhang, X.; Taniguchi, T.; Watanabe, K.; Lanza, M. On the Quality of Commercial Chemical Vapour Deposited Hexagonal Boron Nitride. *Nat. Commun.* **2024**, *15*, 4518.

(16) Tay, R. Y.; Li, H.; Wang, H.; Lin, J.; Ng, Z. K.; Shivakumar, R.; Bolker, A.; Shakerzadeh, M.; Tsang, S. H.; Teo, E. H. T. Advanced Nano Boron Nitride Architectures: Synthesis, Properties and Emerging Applications. *Nano Today* **2023**, *53*, 102011.

(17) Ahmad, P.; Uddin Khandaker, M.; Raza Khan, Z.; Mohd Amin, Y. Synthesis of Boron Nitride Nanotubes via Chemical Vapour Deposition: A Comprehensive Review. *RSC Adv.* **2015**, *5*, 35116−35137.

(18) Okulov, I. V.; Soldatov, I. V.; Sarmanova, M. F.; Kaban, I.; Gemming, T.; Edström, K.; Eckert, J. Flash Joule Heating for Ductilization of Metallic Glasses. *Nat. Commun.* **2015**, *6*, 7932.

(19) Wang, M.; Wang, H.; Gu, Y.; Zhu, M.; Kumar, M.; Liang, J.; Tie, Z.; Ma, J.; Jin, Z. In Situ Generation of Flash Graphene Supported Spherical Bismuth Nanoparticles in Less than 200 Ms for Highly Selective Carbon Dioxide Electroreduction. *ACS Mater. Lett.* **2024**, *6*, 100−108.

(20) Lu, J.; Liu, S.; Liu, J.; Qian, G.; Wang, D.; Gong, X.; Deng, Y.; Chen, Y.; Wang, Z. Millisecond Conversion of Photovoltaic Silicon Waste to Binder-Free High Silicon Content Nanowires Electrodes. *Adv. Energy Mater.* **2021**, *11*, 2102103.

(21) Dong, S.; Song, Y.; Su, M.; Wang, G.; Gao, Y.; Zhu, K.; Cao, D. Flash Joule Heating Induced Highly Defective Graphene towards Ultrahigh Lithium Ion Storage. *Chem. Eng. J.* **2024**, *481*, 147988.

(22) Yang, S.; Wang, H.; Xiong, Y.; Zhu, M.; Sun, J.; Jiang, M.; Zhang, P.; Wei, J.; Xing, Y.; Tie, Z.; Jin, Z. Ultrafast Thermal Shock Synthesis and Porosity Engineering of 3D Hierarchical Cu−Bi Nanofoam Electrodes for Highly Selective Electrochemical CO_2 Reduction. *Nano Lett.* **2023**, *23*, 10140−10147.

(23) Cheng, Y.; Chen, J.; Deng, B.; Chen, W.; Silva, K. J.; Eddy, L.; Wu, G.; Chen, Y.; Li, B.; Kittrell, C.; Xu, S.; Si, T.; Martí, A. A.; Yakobson, B. I.; Zhao, Y.; Tour, J. M. Flash Upcycling of Waste Glass Fibre-Reinforced Plastics to Silicon Carbide. *Nat. Sustain.* **2024**, *7*, 452−462.

(24) Chen, W.; Li, J. T.; Ge, C.; Yuan, Z.; Algozeeb, W. A.; Advincula, P. A.; Gao, G.; Chen, J.; Ling, K.; Choi, C. H.; McHugh, E. A.; Wyss, K. M.; Luong, D. X.; Wang, Z.; Han, Y.; Tour, J. M. Turbostratic Boron−Carbon−Nitrogen and Boron Nitride by Flash Joule Heating. *Adv. Mater.* **2022**, *34*, 2202666.

(25) Chen, W.; Chen, J.; Bets, K. V.; Salvatierra, R. V.; Wyss, K. M.; Gao, G.; Choi, C. H.; Deng, B.; Wang, X.; Li, J. T.; Kittrell, C.; La, N.; Eddy, L.; Scotland, P.; Cheng, Y.; Xu, S.; Li, B.; Tomson, M. B.; Han, Y.; Yakobson, B. I.; Tour, J. M. Battery Metal Recycling by Flash Joule Heating. *Sci. Adv.* **2023**, *9*, No. eadh5131.

(26) Chen, W.; Cheng, Y.; Chen, J.; Bets, K. V.; Salvatierra, R. V.; Ge, C.; Li, J. T.; Luong, D. X.; Kittrell, C.; Wang, Z.; McHugh, E. A.; Gao, G.; Deng, B.; Han, Y.; Yakobson, B. I.; Tour, J. M. Nondestructive Flash Cathode Recycling. *Nat. Commun.* **2024**, *15*, 6250.

(27) Cheng, T.; Bets, K. V.; Yakobson, B. I. Synthesis Landscapes for Ammonia Borane Chemical Vapor Deposition of h-BN and BNNT: Unraveling Reactions and Intermediates from First-Principles. *J. Am. Chem. Soc.* **2024**, *146*, 9318−9325.

(28) McLean, B.; Webber, G. B.; Page, A. J. Boron Nitride Nanotube Nucleation via Network Fusion during Catalytic Chemical Vapor Deposition. *J. Am. Chem. Soc.* **2019**, *141*, 13385−13393.

(29) Xu, T.; Zhang, K.; Cai, Q.; Wang, N.; Wu, L.; He, Q.; Wang, H.; Zhang, Y.; Xie, Y.; Yao, Y.; Chen, Y. Advances in Synthesis and Applications of Boron Nitride Nanotubes: A Review. *Chem. Eng. J.* **2022**, *431*, 134118.

(30) McLean, B.; Webber, G. B.; Page, A. J. Boron Nitride Nanotube Nucleation during Ni-Catalyzed Boron Oxide Chemical Vapor Deposition. *J. Phys. Chem. C* **2019**, *123*, 27875−27883.

(31) Eddy, L.; Shin, J.; Cheng, Y.; Choi, C. H.; Teng, C.; Scotland, P.; Xu, S.; Lathem, A.; Chen, S.; Kittrell, C.; Han, Y.; Tour, J. M. Kilogram Flash Joule Heating Synthesis with an Arc Welder. *ACS Nano* **2024**, *18*, 34207−34218.

(32) Universal Matter. https://www.universalmatter.com/ (accessed Feb 16, 2025).

(33) Kim, S. M.; Hsu, A.; Park, M. H.; Chae, S. H.; Yun, S. J.; Lee, J. S.; Cho, D.-H.; Fang, W.; Lee, C.; Palacios, T.; Dresselhaus, M.; Kim, K. K.; Lee, Y. H.; Kong, J. Synthesis of Large-Area Multilayer Hexagonal Boron Nitride for High Material Performance. *Nat. Commun.* **2015**, *6*, 8662.

(34) Arenal, R.; Ferrari, A. C.; Reich, S.; Wirtz, L.; Mevellec, J.-Y.; Lefrant, S.; Rubio, A.; Loiseau, A. Raman Spectroscopy of Single-Wall Boron Nitride Nanotubes. *Nano Lett.* **2006**, *6*, 1812−1816.

(35) Wang, S.; Levshov, D. I.; Otsuka, K.; Zhang, B.-W.; Zheng, Y.; Feng, Y.; Liu, M.; Kauppinen, E. I.; Xiang, R.; Chiashi, S.; Wenseleers, W.; Cambré, S.; Maruyama, S. Evaluating the Efficiency of Boron Nitride Coating in Single-Walled Carbon-Nanotube-Based 1D Heterostructure Films by Optical Spectroscopy. *ACS Nano* **2024**, *18*, 9917−9928.

(36) Shi, Y.; Hamsen, C.; Jia, X.; Kim, K. K.; Reina, A.; Hofmann, M.; Hsu, A. L.; Zhang, K.; Li, H.; Juang, Z.-Y.; Dresselhaus, M. S.; Li, L.-J.; Kong, J. Synthesis of Few-Layer Hexagonal Boron Nitride Thin Film by Chemical Vapor Deposition. *Nano Lett.* **2010**, *10*, 4134−4139.

(37) Lei, W.; Portehault, D.; Liu, D.; Qin, S.; Chen, Y. Porous Boron Nitride Nanosheets for Effective Water Cleaning. *Nat. Commun.* **2013**, *4*, 1777.

(38) Huang, Y.; Lin, J.; Zou, J.; Wang, M.-S.; Faerstein, K.; Tang, C.; Bando, Y.; Golberg, D. Thin Boron Nitride Nanotubes with Exceptionally High Strength and Toughness. *Nanoscale* **2013**, *5*, 4840−4846.

(39) Zhu, M.; Li, G.; Zhang, X.; Zhai, J.; Gan, S.; Song, X. Boron Nitride Nanosheets Supported Cu_2O Nanoparticles: Synthesis and Catalytic Reduction for 4-Nitrophenol. *J. Inorg. Mater.* **2019**, *34*, 817.

(40) Oliver, W. C.; Pharr, G. M. An Improved Technique for Determining Hardness and Elastic Modulus Using Load and Displacement Sensing Indentation Experiments. *J. Mater. Res.* **1992**, *7*, 1564−1583.